


Electronic and catalytic engineering in two-dimensional vdW metal–organic frameworks through alloying

Cite as: Appl. Phys. Rev. **8**, 031411 (2021); <https://doi.org/10.1063/5.0051219>

Submitted: 23 March 2021 . Accepted: 02 August 2021 . Published Online: 18 August 2021

 Yuxia Shen, Bohan Shan, Christopher Muhich, Srishti Gupta, Han Li, Patrick Hays,  Ying Qin, Shiljashree Vijay, Joseph Winarta, Bin Mu,  Sefaattin Tongay, et al.

COLLECTIONS

 This paper was selected as Featured



View Online



Export Citation



CrossMark

ARTICLES YOU MAY BE INTERESTED IN

[pH sensors based on amino-terminated carbon nanomembrane and single-layer graphene van der Waals heterostructures](#)

Applied Physics Reviews **8**, 031410 (2021); <https://doi.org/10.1063/5.0040442>

[Observation of spatially resolved Rashba states on the surface of \$\text{CH}_3\text{NH}_3\text{PbBr}_3\$ single crystals](#)

Applied Physics Reviews **8**, 031408 (2021); <https://doi.org/10.1063/5.0053884>

[Maximizing spin-orbit torque generated by the spin Hall effect of Pt](#)

Applied Physics Reviews **8**, 031308 (2021); <https://doi.org/10.1063/5.0059171>



Applied Physics
Reviews

Read. Cite. Publish. Repeat.



Electronic and catalytic engineering in two-dimensional vdW metal-organic frameworks through alloying

Cite as: Appl. Phys. Rev. **8**, 031411 (2021); doi: [10.1063/5.0051219](https://doi.org/10.1063/5.0051219)

Submitted: 23 March 2021 · Accepted: 2 August 2021 ·

Published Online: 18 August 2021



View Online



Export Citation



CrossMark

Yuxia Shen,  Bohan Shan, Christopher Muhich, Srishti Gupta, Han Li, Patrick Hays, Ying Qin,  Shiljashree Vijay, Joseph Winarta, Bin Mu, and Sefaattin Tongay 

AFFILIATIONS

School for Engineering of Matter Transport and Energy, Arizona State University, Tempe, Arizona 85287, USA

^{a)}Author to whom correspondence should be addressed: sefaattin.tongay@asu.edu

ABSTRACT

Bimetallic metal-organic framework (MOFs) alloys, in which heterogeneous metal clusters are incorporated into their backbone, are capable of highly selective separations and catalysis. Due to limitations in our fundamental understanding of their alloying, however, established methods result in phase-separated or amorphous two-dimensional (2D) MOFs or lack precise control over alloy ratios. Here, our results demonstrate 2D MOF alloys where metal cation ratios (M^1 and M^2) in $M^1_xM^2_{1-x}$ BDC (M^1 or $M^2 = \text{Zn, Cu, Ni, Co, Fe, Mn}$) can be engineered on demand by controlling the metal salt dissociation constants. Resulting MOF alloys exhibit a highly 2D nature with excellent crystallinity and minute control over metal cation ratios. Our experimental and theoretical results show that their electronic bandgaps and photoexcited carrier lifetimes can be engineered by metal cation alloying. Interestingly, 2D alloyed MOFs enable high-efficiency photocatalytic water reduction performance in Co/Ni MOF alloys owing to the spatially separated metal clusters in 2D MOF alloys.

Published under an exclusive license by AIP Publishing. <https://doi.org/10.1063/5.0051219>

MAIN

Metal-organic frameworks (MOFs) fabricated from a wide array of metal cations offer unique properties and functionalities.^{1–3} For example, transition metals possessing unfilled *d*-orbitals generate coordinatively unsaturated or open metal sites, which are particularly selective in recognizing small molecules⁴ and facilitating carrier transfer in heterogeneous catalysis.⁵ Especially when these three-dimensional (3D) traditional MOFs are synthesized in two-dimensional (2D) form, they offer added functionalities and sensitivity owing to their much enhanced surface-to-volume ratios.^{6–8} In these 2D MOFs, metal clusters and organic linkers are constructed by coordination bonding only in the 2D landscape, while the adjacent layers are bonded via hydrogen bonds or weak van der Waals (vdW) force. Considering the vital role played by the judicious choice of metal cations, MOFs with two different metal types (bimetallic MOFs) enable remarkable improvement in properties analogous to traditional alloying, as long as phase separation can be prevented and alloy ratios can be engineered on demand.

Previously, metal cation alloying in bulk MOFs has only been demonstrated a few times wherein the ratio of the metal cations (composition) was not engineered but set at a given value. By incorporating

secondary metal cation, it was shown it is possible to enhance nitrogen sorption (bimetallic HKUST-1)⁹ or improve the performance of Li-O₂ batteries in bimetallic Mn/Co in MOF-74).¹⁰ Similar alloying approaches can, in principle, open a myriad of possibilities, but there exist great challenges to fabricate 2D MOF alloys, since the steric configuration and coordination numbers of metal cations ultimately determine if the 2D structure can be retained within a stable phase and elemental composition.

Here, we present a systematic approach to synthesize 2D MOF bimetallic alloys with any combination of 3*d* transition metal cations from half-filled Mn (3*d*⁵) to fully occupied Zn (3*d*¹⁰) (Fig. 1) with a controllable amount of alloy ratios. The two different metal ions, “ M^1 ” and “ M^2 ,” are linked with benzene-1, 4-dicarboxylic acid (BDC); therefore, the synthesized 2D MOF alloys are denoted as “ $M^1_xM^2_{1-x}$ BDC” (M^1 or $M^2 = \text{Zn, Cu, Ni, Co, Fe, Mn}$; x value ranging from 0 to 1) [Fig. 1(a)]. The microscopy⁸ and spectroscopy¹¹ studies (Figs. S1 and S2) reveal these synthesized 2D $M^1_xM^2_{1-x}$ BDC layers are highly crystalline and retain their 2D nature at desired alloying ratios. Systematic studies are presented to explain the growth mechanism and dynamics. Additionally, we examine the photocatalytic behavior of our 2D MOF alloys, which revealed that high-efficiency photocatalytic water splitting

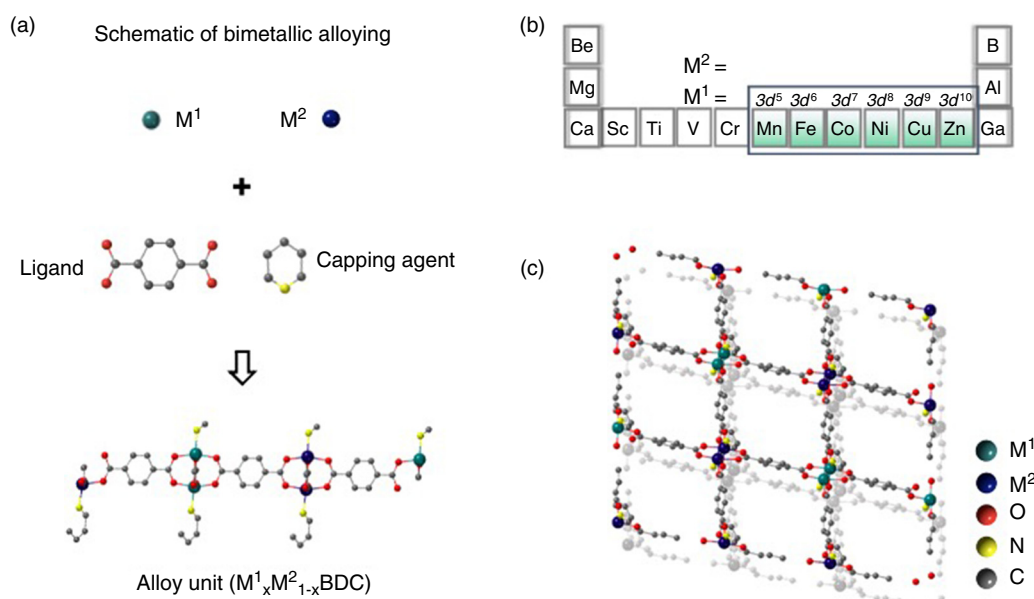


FIG. 1. Schematic structure of 2D vdW MOF alloys ($M^1_xM^2_{1-x}BDC$) and involved metal types in this article. (a) The basic building units in $M^1_xM^2_{1-x}BDC$; (b) involved metal types in partial periodic elemental table; (c) top view of obtained $M^1_xM^2_{1-x}BDC$ with randomly arranged M^1 and M^2 clusters.

can be attained. Overall, these studies introduce the world's first 2D MOFs alloys involving different metal cations and establish how their physical properties change to achieve high-efficiency catalytic devices.

Competitive growth in 2D MOF alloys

As mentioned in Main, the synthesis of uniform 2D MOF alloys is not achievable by arbitrary mixing metal ions. Through our systematic investigation of a $M^1_xM^2_{1-x}BDC$ prototype, we observe a unique competitive growth phenomenon that reveals the formation of uniform 2D MOF crystals with adjustable alloy ratio at large scales.

Before we discuss our successful route to generate fully alloyed 2D MOFs using Co-Ni as the tested material system, we describe our initial attempts to synthesize the MOF alloys using a conventional approach. The existing approach uses BDC, pyridine, and metal salts with identical anions, i.e., Ni and Co chloride ($NiCl_2/CoCl_2 = 1/1$), as precursors. In our studies, we have dissolved $NiCl_2$ and $CoCl_2$ in DMF to obtain a uniform metal cation solution. After adding pyridine into this metal solution, it was mixed with ligand solution dropwise. Typical products from similar growth runs have resulted in a mixture of NiBDC (green) and $Co_{0.21}Ni_{0.79}BDC$ alloy (purple) crystals as shown in Fig. S3(a), while the unreacted Co or Ni cations remained in the solution without participating in the growth process. Careful EDS mapping of Ni-K α and Co-K α has also shown the presence of $Co_{0.21}Ni_{0.79}BDC$ along with NiBDC [Fig. S3(b)]. Even though the $NiCl_2$ and $CoCl_2$ precursors were used at a 1:1 ratio, the presence of Ni-rich $Co_{0.21}Ni_{0.79}BDC$ alloy and NiBDC implies that the reaction constant ($[M^+ \text{ cation}]/[M-O \text{ coordination species}]$) for $NiCl_2$ is far greater than that of $CoCl_2$. More specifically, Ni ions are more reactive with the BDC ligand than Co during the $Ni_xCo_{1-x}BDC$ formation, and only a fraction of Co cations in the solution coordinate into the alloyed structure. These trends can be observed across the entire Co/(Co+Ni)

precursor range used in our growth process, as depicted by solid red dots in Fig. 2(a). Here it is noteworthy to mention that only precursor solutions with over 80% Co cations produced a $CoNiBDC$ alloy structure, and even then the final Co content of the MOF was only 52%. Precursor salt mixtures below 80% $CoCl_2$ always produced separated mixtures consisting of NiBDC and low Co content alloys.

The growth dynamics of 2D MOF alloys is characterized by the different reaction constants between the two metal cations. Here we use odds ratio $OR = [M^1/M^2(Alloy)]/[M^1/M^2(Precursor)]$ as an indicator to illustrate the relative reactivity of M^1 over M^2 cation. Systematic results involving various metal pairs are present in Fig. 2(a). The data in the orange region indicates M^1 has a lower reaction constant than that of M^2 , while the purple region is the opposite. In the case that M^1 and M^2 have comparable reactivities, their OR values fall along the solid diagonal line.

We find that competing growth occurs in other metal pairs as well. Starting from their chloride precursors (MCl_2 , $M = Zn, Cu, Co$, and Ni), the relative competitions between these metal cations are demonstrated in Fig. 2(a). Starting with a 1:1 ratio of bimetal precursors, the relative reactivity of Ni, Co, and Cu are all higher than that of Zn. We presume that electronegativity is a key parameter; however, other effects, such as *d*-orbital configuration and coordination number, should also be considered. Our typical SEM and EDS mapping results [Fig. 2(c)] demonstrate the classic 2D morphology and uniform alloying of these alloys, including $Ni_{0.78}Co_{0.22}BDC$, $Ni_{0.92}Zn_{0.08}BDC$, $Cu_{0.50}Co_{0.50}BDC$, and $Cu_{0.89}Zn_{0.11}BDC$.

How can one achieve better control over alloy ratios using a molar mixture of metal cation precursors and prevent the formation of NiBDC or CoBDC? Since $NiCl_2$ precursors are more reactive than $CoCl_2$, we have substituted the Ni chloride precursor with the less soluble Ni acetylacetonate salt ($acac = CH_3-O-O-CH_3$). This, in principle, provides fewer reactive Ni precursor ions at any given time, enabling similar Co

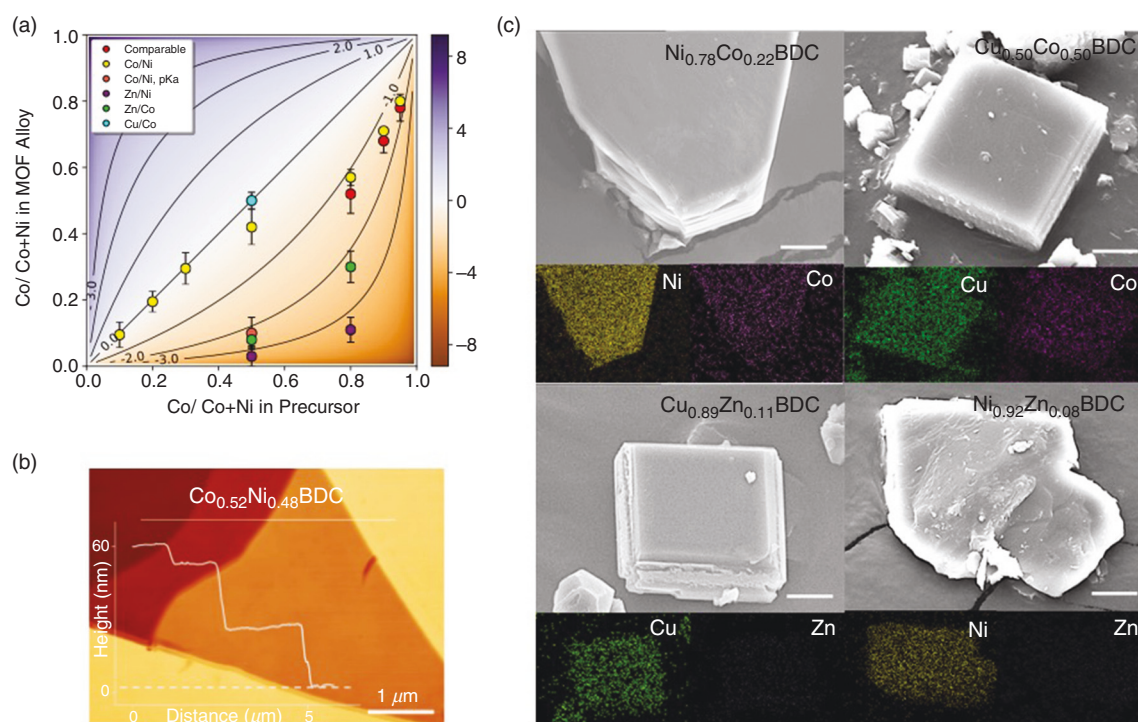


FIG. 2. The featured competitive growth in 2D MOF alloys. (a) The relative competition between M^1 and M^2 , M^1 or $M^2 = \text{Ni, Co, Cu, and Zn}$. Calculated odds ratio of M^1/M^2 in alloys over M^1/M^2 in precursors are displayed as one diagonal line and curves with denoted values. Besides, the colored competitive spectrum based on log odds ratio values indicates the superiority degree between M^1/M^2 ; (b) typical AFM height profile of $\text{Ni}_{0.52}\text{Co}_{0.48}\text{BDC}$ few layers demonstrate the vdW nature; (c) versatility of the proposed synthesis strategy to produce 2D MOF alloys by substituting $M^1/M^2 = \text{Zn/Cu, Zn/Ni, Cu/Ni, and Cu/Co}$. SEM and EDS mapping images suggest their lamellar morphology and uniform composition.

and Ni coordination rates with the BDC molecules. This should result in a MOF alloy where the metal ratios are dictated by the initial precursor quantities. These results are shown by yellow dots in Fig. 2(a). It can be clearly seen that the resulting $\text{Co}/(\text{Co}+\text{Ni})$ alloy ratios closely follow the ratio of Co to Ni precursor used, thereby enabling us to synthesize uniform $\text{Ni}_x\text{Co}_{1-x}\text{BDC}$ alloys with continuous alloy ratios ($x = 0.10, 0.20, 0.30, 0.41, 0.57, 0.71, 0.80$). It is noteworthy that even when the fraction of the Co precursor is low, using $\text{Ni}(\text{acac})_2$, with its small dissociation constant, leads to predictable alloy ratios. However, we note that when the CoCl_2 precursor fraction is high (80% and above), the alloy does deviate from linearity while still remaining capable of achieving a high Co concentration of 2D MOF alloys. Overall, the combination of CoCl_2 and $\text{Ni}(\text{acac})_2$, which have similar disassociation constants, produces a single phase, meaning only 2D MOF alloys, without NiBDC or CoBDC segments. Additionally, the contribution of pyridine on the growth of crystalline 2D CoNiBDC alloys is indispensable. A detailed discussion about the roles of pyridine is involved in [supplementary material](#) and Fig. S4.

Tunable band gaps and electron transfer between hetero clusters

Similar to alloying in traditional or 2D material systems,^{12–14} alloying 2D MOFs enables one to engineer the physical properties of the synthesized systems such as the bandgap. Here, we have performed

UV-Vis absorption spectroscopy measurements [Fig. 3(a)] on $\text{Co}_x\text{Ni}_{1-x}\text{BDC}$ ($x = 0, 0.12, 0.31, 0.72$, and 1) and performed comprehensive theoretical studies to understand how increasing Co concentration influences their behavior [Fig. 3(b) and Fig. S5]. Parent NiBDC ($x = 0$) exhibited two main absorption peaks located at 1.84 eV and 3.05 eV, while CoBDC ($x = 1$) has two predominant transitions around 2.27 eV and 3.83 eV. We find that as the Co concentration (x) increases, the absorbance spectra of $\text{Co}_x\text{Ni}_{1-x}\text{BDC}$ gradually shifts from NiBDC to CoBDC like features, instead of a simple addition of two pure MOFs. This implies that the concentrations of Co and Ni cations and their interaction are playing key roles in the electronic band structure of $\text{Co}_x\text{Ni}_{1-x}\text{BDC}$. The interaction of Co and Ni cations through BDC linker can also be evidenced by our x-ray photoelectron spectroscopy (XPS) measurements (Fig. S6). For example, in $\text{Co}_{0.52}\text{Ni}_{0.48}\text{BDC}$, Ni $2p_{3/2}$ peak shifted from 854.7 eV (NiBDC) to 856.1 eV (alloy) compared to NiBDC , while the binding energy of Co $2p_{3/2}$ varied in alloy by 500 meV compared to CoBDC .

Furthermore, the Tauc plots of $\text{Co}_x\text{Ni}_{1-x}\text{BDC}$ ($x = 0, 0.12, 0.31, 0.72$, and 1) have been analyzed to investigate their bandgap evolution, as shown in Fig. 3(c) and Fig. S7. NiBDC ($x = 0$) exhibits an optical bandgap at 3.75 eV, and increasing Co concentration ($x > 0$) leads to a continuous reduction in its bandgap decreasing by 450 ~550 meV until it reaches 3.11 eV for CoBDC or $x = 1$. It can be seen from E_g vs Co fraction (x) curves that the correlation is not linear, meaning increasing x does not result in a linear change in the bandgap. Instead,

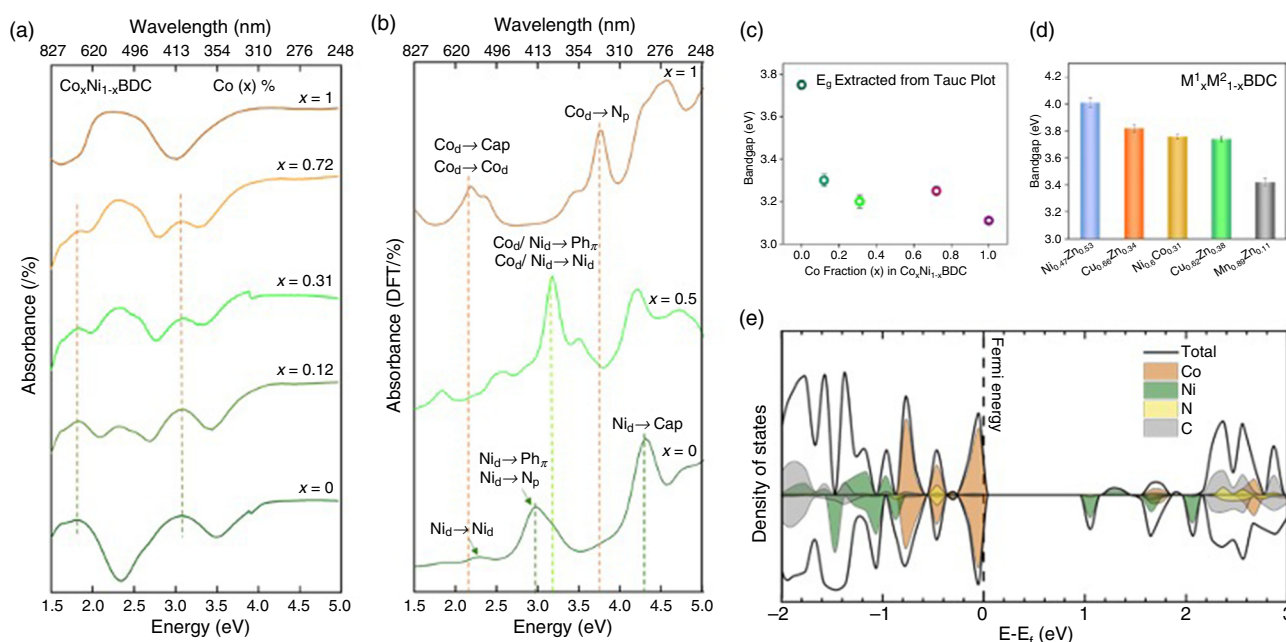


FIG. 3. Optical properties of $\text{M}^1_x\text{M}^2_{1-x}\text{BDC}$ alloys. (a) UV-Vis absorbance spectroscopy spectra of $\text{Co}_x\text{Ni}_{1-x}\text{BDC}$ ($x = 0, 0.34, 0.52, 0.66, 0.78$, and 1) crystals; (b) DFT calculated absorbance spectra of NiBDC , $\text{Co}_{0.5}\text{Ni}_{0.5}\text{BDC}$, and CoBDC ; (c) and (d) extracted optical bandgap values of $\text{Co}_x\text{Ni}_{1-x}\text{BDC}$ and 2D MOF alloys with other metal pairs; (e) projected density of states (DOS) of $\text{Co}_{0.5}\text{Ni}_{0.5}\text{BDC}$.

a small amount of Co incorporation into NiBDC host matrix causes large changes (small x limit). The behavior is referred to as negative band bowing and implies that the band structure is mainly dictated by contributions from the Co orbitals, which will be discussed in the section Theoretical understanding of alloying in 2D MOFs. Here, we also show other achieved bandgap parameters for other 2D MOF alloys by designing metal pairs for the first time, as shown in Fig. 3(d). $\text{Mn}_{0.89}\text{Zn}_{0.11}\text{BDC}$ has the smallest bandgap (3.42 eV), while $\text{Ni}_{0.47}\text{Zn}_{0.53}\text{BDC}$ holds the largest band gap (4.01 eV) among all these types of alloys. These results confirmed the key role of metal types in the determination of MOF bandgap, which was only theoretically predicted^{3,15,16} before.

Theoretical understanding of alloying in 2D MOFs

To understand the electronic behavior of the 2D MOF systems, we performed density functional theory (DFT) analysis of the single metal and 50/50% Co/Ni ($\text{Co}_{0.5}\text{Ni}_{0.5}\text{BDC}$) alloyed materials. All calculations were completed in VASP^{17,18} using the HSE06¹⁹ density functional, with 10% exact exchange. The wavefunction was constructed by a summation of plane waves with energies up to 1000 eV, and the Brillion Zone was sampled on a $4 \times 4 \times 1$ Γ -point centered Monkhorst-Pack grid. The alloy was modeled by a supercell consisting of $1 \times 2 \times 1$ primitive cells with two Ni or two Co atoms paired. We attempted to construct the alloy with mixed metal centers, but this was unstable. The wavefunction of NiCoBDC was sampled on a $4 \times 2 \times 1$ k-point grid.

The NiBDC and CoBDC band edges are composed of metal d states, with additional mixing of the organic states below and above the valence and conduction band edges, respectively, as shown in

Fig. S5. Additionally, Co and Ni d states form a mid-gap state 1.28 and 1.25 eV above the valence band maximum. These states give rise to a band edge-to-band edge gap of 2.83 eV and 3.04 eV and a mid-gap-state-to-band edge gap of 1.37 and 1.87 eV for Co and Ni, respectively. While these band gaps are substantially lower than the experimentally measured bandgap, these are not the photoactive states. The calculated absorption spectra [Fig. 3(b)], calculated using a frequency-dependent complex dielectric function, shows adsorption maxima at 3.74 and 4.30 eV for Co and Ni, respectively. Applying Tauc plot analysis of the calculated adsorption spectrum results in an “apparent” bandgap of 3.25 and 4.04 eV, which matches well with the experimental values of 3.1 and 3.75 eV.

The band edge-to-band edge absorption between 1.5 and 2.25 eV is very weak for NiBDC , as is seen by the lack of adsorption in the calculated spectra at the true bandgap, but more significant for CoBDC . We attribute the poor adsorption in Ni to a limited coupling between the states near the band edges because of their similar Ni d-states e_{2g} symmetries. Although the metal transition in CoBDC ($\text{Co}_d \rightarrow \text{Co}_d$) is insufficient as well, the slight mixing of Co_d with chelating N and C states from the capping agent (noted as “ $\text{Co}_d \rightarrow \text{Cap}$ ” near the orange spectrum) leads to an increment in the absorption.

The major absorption peaks are located at ~ 2.98 and 4.30 eV for NiBDC and 3.75 and 4.76 for CoBDC . Both result from electron excitation from the metal d state to the benzene π states of the linker molecules and the N and C states of the capping agents. Upon excitation, electrons are expected to quickly relax from the benzene states through the continuum of states to the metal d-states at the conduction band edge. The poor coupling between the band edge states suggests that electrons and holes at those states should have long lifetimes, and thus be excellent for driving chemical reactions.

The $\text{Co}_{0.5}\text{Ni}_{0.5}\text{BDC}$ alloy retains many of the distinctive electronic characteristics of both NiBDC and CoBDC, rather than a blending of behavior. As seen in the density of states (DOS) plot and the adsorption spectra, the peaks associated with Ni and Co centers from the pure phases are retained though slightly shifted, which parallels the experimental findings. We attribute this to the fact that each metal dimer is composed of either Co or Ni and the metal centers are relatively far from each other. The slight changes to the adsorption energies from the un-alloyed material are attributed to altered lattice parameters and small redistribution of electron densities around each metal center due to the electronic communication. We do note that the major adsorption peak in NiCoBDC is a combination of metal d-benzene π transitions and Co to Ni transition. The latter is unique to the mixed $\text{Co}_{0.5}\text{Ni}_{0.5}\text{BDC}$ alloy because of the presence of two metal centers.

The $\text{Co}_{0.5}\text{Ni}_{0.5}\text{BDC}$ alloy is expected to demonstrate a unique density of states [Fig. 3(e)] from its parent materials because of the alignment of its bands. The highest occupied band is mostly Co in character, while the lowest unoccupied band is Ni in character. This results in the lowest energy significant excitation arising from Co d-states to benzene π -states and Co to Ni transition, though we expect the former to be more strongly coupled. The lower energy of the Ni conduction band states as compared to the Co states results in the excited electron relaxing to and localizing on Ni centers. Similarly, the photogenerated hole localizes on the Co centers, from where it originated, leaving the electron and the whole physically separated. This further increases quasi-particle lifetime as compared to the unalloyed MOF by physically separating the excited electrons and holes, thus

decreasing the transition dipole moment, and the recombination probability.

Photocatalytic water splitting

The presence of two different, spatially separated metal clusters and the calculation results suggests that photo-excited polarons are rapidly split into electrons and holes. This behavior hints at the possibility of long photo-excited carrier lifetimes and potentially high catalytic performance. We have carried out systematic photocatalytic water splitting studies on several samples from $\text{Co}_{0.52}\text{Ni}_{0.48}\text{BDC}$ and compared our results to those from parent CoBDC and NiBDC sheets to elucidate the role of two metal cation alloys and their catalytic performance. In a typical measurement, the working electrode made of MOF catalyst film was subject to photons at select energies from 325 nm to 625 nm. These MOF catalyst films were deposited onto the conductive side of ITO glass [Fig. 4(a)], and the thickness of the catalyst film is determined by SEM images [Fig. 4(c)]. Next, the photo-generated electrons pass through an external circuit and are recorded by a potentiostat setup [Fig. 4(b)]. Finally, the photocatalysis performance is evaluated by the photocurrent density as well as the incident photon to current conversion efficiency (IPCE).

The comparison of photocurrent densities of $\text{Co}_{0.52}\text{Ni}_{0.48}\text{BDC}$, CoBDC, and NiBDC is presented in Fig. 4(d). Under the white light irradiation, the photon-generated current density with a maximum value in $\text{Co}_{0.52}\text{Ni}_{0.48}\text{BDC}$ is $1.94 \mu\text{A}/\text{cm}^2$. CoBDC and NiBDC only hold 1.0 and $0.17 \mu\text{A}/\text{cm}^2$, respectively. Similarly, the improved photocatalytic behavior of $\text{Co}_{0.52}\text{Ni}_{0.48}\text{BDC}$ is verified in the comparison of

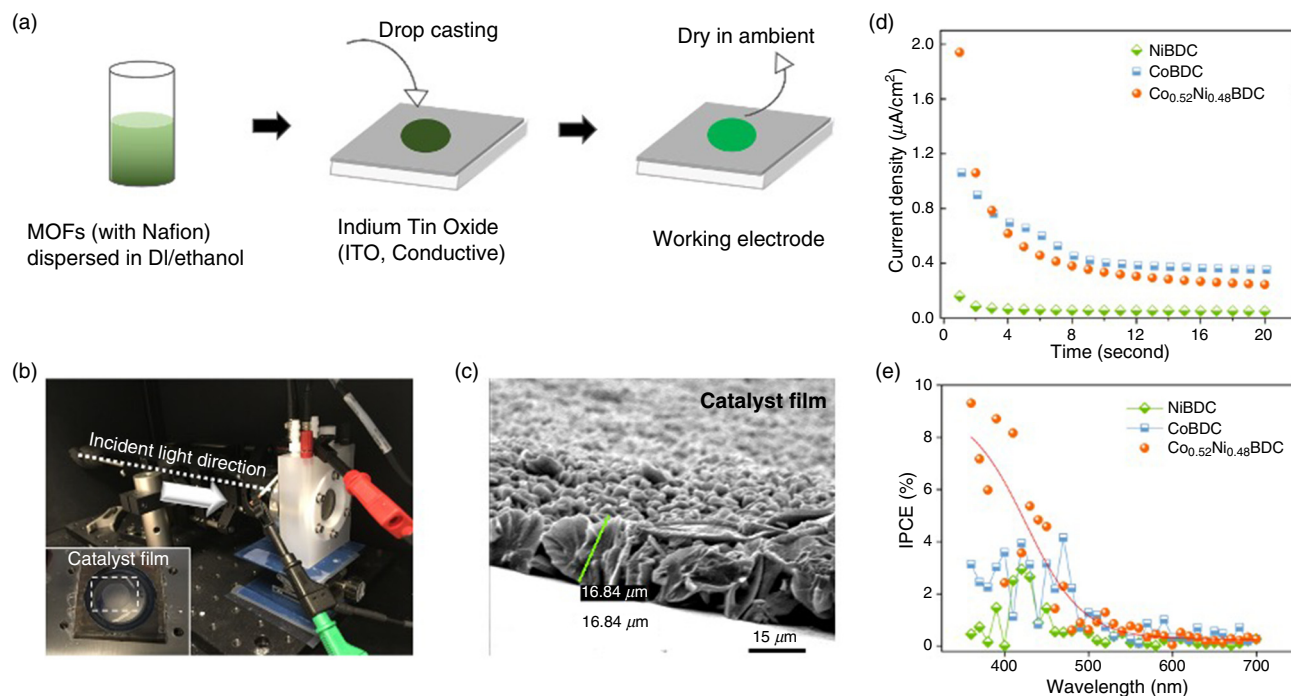


FIG. 4. The photocatalytic performance of $\text{Co}_{0.52}\text{Ni}_{0.48}\text{BDC}$, CoBDC, and NiBDC. (a) Schematic illustration of the deposition of MOF film; (b) photo of photocatalytic measurement setup; (c) SEM morphology of working electrode with measured thickness; (d) photon-generated current density after white light irradiation for 30 s; (e) incident photon to current conversion efficiency (IPCE) as a function of incident photon wavelength.

IPCE plots [Fig. 4(e)]. The maximum value of IPCE (IPCE_{max}) of the alloy is 9.3% with the incident energy of 3.45 eV. And the IPCE value retains higher than 5% within the incident light wavelength of 450 nm. This is more than twice the IPCE_{max} of CoBDC and NiBDC, 4.1% and 3.0%, respectively. Here, we note that the photo-generated current of the Co/Ni-BDC sample decays slightly faster with time than that of CoBDC, as shown in Fig. 4(d). We attribute this to slightly reduced crystalline quality of CoNiBDC samples compared with CoBDC arising from increased defects/crystallinity mediated by Ni incorporation (with faster reaction rates).

The enhanced photon to current conversion in the bimetallic alloys is attributed to the electron-hole separation caused by the presence of two dissimilar metal centers, which localizes the holes and electrons on two distinct and physically separated sites. As described above, the DFT electronic structure shows that the photoexcited electrons and hole of $\text{Co}_{0.52}\text{Ni}_{0.48}\text{BDC}$ localize on the physically separated Co/Ni metal centers [Fig. 3(e)], and that these states are only weakly coupled, in contrast to the single metal MOFs, which show stronger coupling [Fig. 3(b)]; thus, the charge carriers are expected to separate and remain separated. The theoretical charge carrier separation of $\text{Co}_{0.52}\text{Ni}_{0.48}\text{BDC}$ overcomes the well-known photocatalytic limitation of electron-hole pair recombination.^{20–22}

In order to confirm our conclusion of photocatalytic activity, we have conducted electrochemical impedance spectroscopy (EIS). The EIS Nyquist plot represents a measure of the rate of the reaction on the photocatalyst, and, thus, a smaller radius reflects an effective separation of charge carriers.^{23–25} The EIS Nyquist plots of NiBDC, CoBDC, and $\text{Co}_{0.52}\text{Ni}_{0.48}\text{BDC}$ and the equivalent circuit are shown in Fig. S9. Among these three catalysts, bimetallic CoNiBDC displays the smallest semicircle, which indicates the highest photocatalytic activity.²⁶ Based on the equivalent circuit, such high photocatalytic performance is ascribed to the lower charge transfer resistance and space charge capacitance, which allows efficient charge separation of electron/hole pairs. By contrast, 2D MOFs with mono-type metal cluster have more difficulty reaching the semiconductor/electrolyte interface where the photocatalytic reaction takes place, and more electrons have the possibility of recombining before reacting.

This conclusion is further supported by the electrochemical impedance spectroscopy (EIS) results [Fig. 4(d)], in which HP-CdS exhibits the smallest radius, revealing the lowest charge-transfer resistance.

CONCLUSION

We have demonstrated a scalable synthesis of 2D vdW MOF alloys with tunable metal type and ratio. The presented methodology is universal for obtaining 2D $\text{M}^1\text{M}^2\text{BDC}$ (M^1 or $\text{M}^2 = \text{Zn}, \text{Cu}, \text{Ni}, \text{Co}, \text{Fe},$ and Mn) layers with vdW nature and great crystallinity. Overall results highlight the importance of metal cation precursor selection to ensure similar reaction rates to achieve 2D MOF alloys with well-engineered alloy composition and avoid the formation of binary phases. Using experimental and theoretical simulations, for the first time, our results show that alloying in 2D MOFs allows for engineering their physical behavior and offer insight into the mechanism behind the bandgap engineering. Enhanced catalytic performance on MOF alloy $\text{Co}_{0.52}\text{Ni}_{0.48}\text{BDC}$, in comparison to CoBDC and NiBDC, suggests the extended electron/hole lifetime by spatial separation in alloys. Overall, our findings are anticipated to open new avenues of

fine control over the synthesis of 2D MOF alloys and to offer fundamental insights for the potential photocatalytic applications of bimetallic 2D MOF alloys.

EXPERIMENTAL DETAILS

Growth procedures

$\text{Zn}(\text{NO}_3)_2 \cdot 6\text{H}_2\text{O}$, $\text{Cu}(\text{NO}_3)_2 \cdot 3\text{H}_2\text{O}$, $\text{NiCl}_2 \cdot 6\text{H}_2\text{O}$, $\text{Ni}(\text{acac})_2$, $\text{CoCl}_2 \cdot 6\text{H}_2\text{O}$, $\text{MnCl}_2 \cdot 4\text{H}_2\text{O}$, FeCl_3 , benzene-1,4-dicarboxylic acid (H_2BDC), pyridine, and acetone were purchased from Sigma-Aldrich without further purification. N, N-Dimethylformamide (DMF) was purchased from Fisher Scientific.

$\text{CoCl}_2 \cdot 6\text{H}_2\text{O}$ and $\text{NiCl}_2 \cdot 6\text{H}_2\text{O}$ were mixed at a certain molar ratio with a total 1.33 mmol. The mixed metal salts and pyridine (0.18 ml) were dissolved in 10 ml DMF to form the first precursor solution. In the second container, 2 mmol H_2BDC was dissolved in 5 ml DMF. Both solutions were then bath-sonicated for 2 min. The first precursor solution was added into the second container dropwise. The mixture solution was transferred into a hydrothermal reactor, which is sealed in an autoclave with a Teflon interior. The reaction was carried out in an isotherm oven at 120°C for 24 h. After the reaction stops, crystals were scooped out and cleaned by washing using fresh DMF and acetone for three times, respectively. At last, collected samples were dried in vacuum oven at 100°C for 10 h.

Other MOF alloys were synthesized via the similar procedure, except for replacing $\text{NiCl}_2 \cdot 6\text{H}_2\text{O}$ and $\text{CoCl}_2 \cdot 6\text{H}_2\text{O}$ with other metal precursors accordingly.

Characterization

The imaging of 2D MOF alloys was performed using a Philips XL30 environmental scanning electron microscope (SEM) at a voltage of 10 kV with the assistance of Au sputter coating. The Raman spectroscopy measurements were taken using a Renishaw InVia Raman microscope under 100 objective lens with 488 nm laser at $37.5 \mu\text{W}$ as the excitation source. AFM topography was conducted in the contact mode, in which the scan size was 256×256 , and the scanning speed was set to 1 Hz. Data were analyzed by Gwyddion software. The powder XRD of samples was collected using a PANalytical Aeris powder x-ray diffractometer with $\text{Cu K}\alpha$ radiation ($\lambda = 1.542 \text{ \AA}$) with a scan step of 0.02° . Optical properties were measured on a UV-Vis-Lambda 950 spectrometer with an incident photon wavelength from 200 to 800 nm. $\text{M}^1_x\text{M}^2_{1-x}\text{BDC}$ samples were collected between two pieces of clean sapphire to form a sandwich configuration. The whole part was stabilized with adhesive tape around the outside of the sapphires. The optical properties of blank sapphires were pre-measured as the baseline.

Theoretical simulations

All quantum mechanical calculations were conducted using periodic boundary condition as implemented in the Vienna *Ab initio* Simulation Package (VASP)^{17,18} using the HSE06¹⁹ density functional, with 10% exact exchange. The wavefunction was constructed by a summation of plane waves with energies up to 1000 eV, and the Brillion Zone was sampled on a $4 \times 4 \times 1$ Γ -point centered Monkhorst-Pack grid. The wavefunction of NiCoBDC was sampled on a $4 \times 2 \times 1$ k-point grid. Projector augmented wavefunctions (PAW) were used to reduce the computational cost. All structures

were fully relaxed. Frequency-dependent complex dielectric function was calculated as outlined by M. Fox.²⁷

SUPPLEMENTARY MATERIAL

See the [supplementary material](#) for more information that supports the findings of this study, including morphology and structure of 2D MOF alloys, phase separation, roles of capping agent, DFT calculation, optical properties, and electrochemical impedance spectroscopy.

AUTHORS' CONTRIBUTIONS

Y.S. and B.S. conducted all the synthesis of MOF crystals and structural analyses. H.L., Y.Q., S.V., and J.W. performed optical characterization and EDS elemental mapping. Y.S. conducted the rest of the measurements. C.M. and S.G. provided DFT calculation and its analyses. Y.S., C.M., P.H., B.M., and S.T. wrote the manuscript. S.T. supervised all the research. All authors reviewed the manuscript prior to its submission.

ACKNOWLEDGMENTS

S.T. acknowledges support from Grant No. DOE-SC0020653, NSF DMR Grant No. 1552220, DMR Grant Nos. 1904716 and 1955889, and NSF CMMI Grant Nos. 1825594 and 1933214. S.T. also acknowledges support from Applied Materials Inc. C.L.M. and S.G. acknowledge support from the National Science Foundation Nanosystems Engineering Research Center for Nanotechnology-Enabled Water Treatment (NEWT; Grant No. ERC-1449500). Calculations were conducted in part on the Extreme Science and Engineering Discovery Environment (XSEDE), supported by NSF (Grant No. ACI-1548562), through the Bridges high-performance computer at the Pittsburgh Supercomputing Center (allocation ECD190001). S.T. also acknowledges NSF ECCS 2052527 and DMR 2111812 for spectroscopy and electrical characterizations.

DATA AVAILABILITY

The data that support the findings of this study are available within the article and its [supplementary material](#).

REFERENCES

- ¹S. Yang, X. Lin, W. Lewis, M. Suyetin, E. Bichoutskaia, J. E. Parker, C. C. Tang, D. R. Allan, P. J. Rizkallah, P. Hubberstey, N. R. Champness, K. M. Thomas, A. J. Blake, and M. Schröder, *Nat. Mater.* **11**, 710 (2012).

- ²J. A. Mason, J. Oktawiec, M. K. Taylor, M. R. Hudson, J. Rodriguez, J. E. Bachman, M. I. Gonzalez, A. Cervellino, A. Guagliardi, C. M. Brown, P. L. Llewellyn, N. Masciocchi, and J. R. Long, *Nature* **527**, 357 (2015).
- ³L. J. Wang, H. Deng, H. Furukawa, F. Gándara, K. E. Cordova, D. Peri, and O. M. Yaghi, *Inorg. Chem.* **53**(12), 5881–5883 (2014).
- ⁴H. Furukawa, K. E. Cordova, M. O'Keeffe, and O. M. Yaghi, *Science* **341**(6149), 1230444 (2013).
- ⁵S. Zhao, Y. Wang, J. Dong, C.-T. He, H. Yin, P. An, K. Zhao, X. Zhang, C. Gao, L. Zhang, J. Lv, J. Wang, J. Zhang, A. M. Khattak, N. A. Khan, Z. Wei, J. Zhang, S. Liu, H. Zhao, and Z. Tang, *Nat. Energy* **1**, 16184 (2016).
- ⁶Q. Jiang, P. Xiong, J. Liu, Z. Xie, Q. Wang, X.-Q. Yang, E. Hu, Y. Cao, J. Sun, Y. Xu, and L. Chen, *Angew. Chem. Int. Ed.* **59**(13), 5273–5277 (2020).
- ⁷C. Li, X. Hu, W. Tong, W. Yan, X. Lou, M. Shen, and B. Hu, *ACS Appl. Mater. Interfaces* **9**(35), 29829–29838 (2017).
- ⁸M. Zhao, Q. Lu, Q. Ma, and H. Zhang, *Small Methods* **1**(1–2), 1600030 (2017).
- ⁹M. A. Gotthardt, R. Schoch, S. Wolf, M. Bauer, and W. Kleist, *Dalton Trans.* **44**(5), 2052–2056 (2015).
- ¹⁰S. H. Kim, Y. J. Lee, D. H. Kim, and Y. J. Lee, *ACS Appl. Mater. Interfaces* **10**(1), 660–667 (2018).
- ¹¹Y. Shen, B. Shan, H. Cai, Y. Qin, A. Agarwal, D. B. Trivedi, B. Chen, L. Liu, H. Zhuang, B. Mu, and S. Tongay, *Adv. Mater.* **30**(52), 1802497 (2018).
- ¹²K. Wu, M. Blei, B. Chen, L. Liu, H. Cai, C. Brayfield, D. Wright, H. Zhuang, and S. Tongay, *Adv. Mater.* **32**(17), 2000018 (2020).
- ¹³B. Huang, M. Yoon, B. G. Sumpter, S.-H. Wei, and F. Liu, *Phys. Rev. Lett.* **115**(12), 126806 (2015).
- ¹⁴J. Kang, S. Tongay, J. B. Li, and J. Q. Wu, *J. Appl. Phys.* **113**(14), 143703 (2013).
- ¹⁵J. Castells-Gil, N. M. Padial, N. Almora-Barrios, J. Albero, A. R. Ruiz-Salvador, J. González-Platas, H. García, and C. Martí-Gastaldo, *Angew. Chem. Int. Ed.* **57**(28), 8453–8457 (2018).
- ¹⁶M. A. Syzgantseva, C. P. Ireland, F. M. Ebrahim, B. Smit, and O. A. Syzgantseva, *J. Am. Chem. Soc.* **141**(15), 6271–6278 (2019).
- ¹⁷G. Kresse and J. Furthmüller, *Phys. Rev. B* **54**(16), 11169 (1996).
- ¹⁸G. Kresse and J. Furthmüller, *Comput. Mater. Sci.* **6**(1), 15–50 (1996).
- ¹⁹J. Heyd, G. E. Scuseria, and M. Ernzerhof, *J. Chem. Phys.* **124**(21), 219906 (2006).
- ²⁰Q. Li, B. Guo, J. Yu, J. Ran, B. Zhang, H. Yan, and J. R. Gong, *J. Am. Chem. Soc.* **133**(28), 10878–10884 (2011).
- ²¹W. Wang, X. Xu, W. Zhou, and Z. Shao, *Adv. Sci.* **4**(4), 1600371 (2017).
- ²²C. Chu, Q. Zhu, Z. Pan, S. Gupta, D. Huang, Y. Du, S. Weon, Y. Wu, C. Muhich, E. Stavitski, K. Domen, and J.-H. Kim, *Proc. Natl. Acad. Sci. USA* **117**(12), 6376–6382 (2020).
- ²³S. Li, K. Ji, M. Zhang, C. He, J. Wang, and Z. Li, *Nanoscale* **12**(17), 9533–9540 (2020).
- ²⁴W. Zhan, L. Sun, and X. Han, *Nano-Micro Lett.* **11**(1), 1 (2019).
- ²⁵A. Murali, P. K. Sarswat, and H. Y. Sohn, *Mater. Today Chem.* **11**, 60–68 (2019).
- ²⁶J. Ângelo, P. Magalhães, L. Andrade, and A. Mendes, *Appl. Surf. Sci.* **387**, 183–189 (2016).
- ²⁷M. Fox, “Optical Properties of Solids,” American Association of Physics Teachers (Oxford University Press, 2002).